

## Diffraction of *P*, *S* and Rayleigh waves by three-dimensional topographies

F. Luzón,<sup>1,2</sup> F. J. Sánchez-Sesma,<sup>3,4</sup> J. L. Rodríguez-Zúñiga,<sup>4</sup> A. M. Posadas,<sup>1,2</sup> J. M. García,<sup>1,2</sup> J. Martín,<sup>1,2</sup> M. D. Romacho<sup>1,2</sup> and M. Navarro<sup>1,2</sup>

<sup>1</sup>Departamento de Física Aplicada, Universidad de Almería, Cañada de San Urbano s/n, 04120 Almería, Spain. E-mail: fluzon@filabres.ualm.es

<sup>2</sup>Instituto Andaluz de Geofísica y Prevención de Desastres Sísmicos, Universidad de Granada, 18080 Granada, Spain

<sup>3</sup>Instituto de Ingeniería, UNAM, Cd. Universitaria, Apdo. 70–472, Coyoacán 04510, México D.F., Mexico

<sup>4</sup>Centro de Investigación Sísmica, A.C.Carr. al Ajusco 203, Col. H. Padierna, Tlalpan 14200, México D.F., Mexico

Accepted 1997 January 21. Received 1997 January 7; in original form 1996 July 19

### SUMMARY

The diffraction of *P*, *S* and Rayleigh waves by 3-D topographies in an elastic half-space is studied using a simplified indirect boundary element method (IBEM). This technique is based on the integral representation of the diffracted elastic fields in terms of single-layer boundary sources. It can be seen as a numerical realization of Huygens' principle because diffracted waves are constructed at the boundaries from where they are radiated by means of boundary sources. A Fredholm integral equation of the second kind for such sources is obtained from the stress-free boundary conditions. A simplified discretization scheme for the numerical and analytical integration of the exact Green's functions, which employs circles of various sizes to cover most of the boundary surface, is used.

The incidence of elastic waves on 3-D topographical profiles is studied. We analyse the displacement amplitudes in the frequency, space and time domains. The results show that the vertical walls of a cylindrical cavity are strong diffractors producing emission of energy in all directions. In the case of a mountain and incident *P*, *SV* and *SH* waves the results show a great variability of the surface ground motion. These spatial variations are due to the interference between locally generated diffracted waves. A polarization analysis of the surface displacement at different locations shows that the diffracted waves are mostly surface and creeping waves.

**Key words:** diffraction, numerical techniques, synthetic seismograms, topography, wave propagation.

### INTRODUCTION

Local conditions of topography and geology can produce important changes in the ground motion during earthquakes. One way to estimate these local effects is carried out by means of empirical methods, which are based on the analysis and treatment of seismic records (for a review, see Aki 1988). On the other hand, numerical methods are helpful for understanding the origin of these local effects. This subject has been dealt with as a problem of diffraction of elastic waves [see e.g. Sánchez-Sesma (1996) for a review]. During the last two decades there has been a significant research effort, which has produced many relevant analytical and numerical solutions. Moreover, the recent advances in computer sciences allow for the study of more realistic configurations and even for the inclusion of source and path effects in the simulations (e.g. Fäh *et al.* 1994; Luzón *et al.* 1995; Olsen, Archuleta & Matarese

1995). However, there is room for both improvement and simplification of existing procedures in order to reduce the gap between research and applications. The bulk of the research in this field deals with 2-D configurations. In fact, nowadays most of the developed techniques are being extended to compute more complicated problems such as the 3-D response of 2-D configurations, the so-called 2.5-D problem (e.g. Furumara & Takenaka 1996; Takenaka, Kennett & Fujiwara 1996), and 3-D structures (e.g. Clouteau & Aubry 1995; Luzón & Sánchez-Sesma 1995; Bouchon & Barker 1996).

In this work we use a single-layer boundary integral representation for the diffracted waves to study the diffraction of elastic waves by 3-D topographical structures. Therefore, diffracted waves are built up at the boundaries from where they are radiated. We can locate the sources precisely at the boundary surface because the singularities of Green's functions are integrable (see e.g. Manolis & Beskos 1988). The uncer-

tainty that appears in other approaches (see e.g. Sánchez-Sesma & Rosenblueth 1979) about the location of the sources with their singularities placed outside the region of interest is thus eliminated. This method can be classified as an indirect boundary element method (IBEM) because the problem is formulated in terms of boundary force densities. Source strengths must first be obtained in order to evaluate the diffracted field. This approach can be seen therefore as a numerical realization of Huygens' principle. It differs from the direct boundary element method, where the unknowns are the boundary values of displacements and tractions. Both formulations are closely related and it can be shown that they are mathematically equivalent (Sánchez-Sesma & Campillo 1991). The IBEM has been applied to study the diffraction of elastic waves by 2-D topographical irregularities and 2-D alluvial valleys by Sánchez-Sesma & Campillo (1991) and Sánchez-Sesma, Ramos-Martínez & Campillo (1993), respectively. Using the same technique Pedersen, Maupin & Campillo (1996) studied the 3-D diffraction by 2-D multilayered structures. Sánchez-Sesma & Luzón (1995) also applied the IBEM to study 3-D alluvial valleys.

In the following we present the integral representation used in our technique to describe the elastic displacement and how a system of linear equations is obtained by means of a discretization process of the boundary surfaces. We subsequently compare some results for a hemispherical cavity with those obtained by other authors, and finally we study some examples of diffraction of *P*, *S* and Rayleigh waves by 3-D topographies.

**INTEGRAL REPRESENTATION**

Let us consider a continuous surface *S*, finite or infinite in the Euclidean space. If an elastic material occupies the adjacent space, then a harmonic displacement field originated in *S* can be written, neglecting body forces, by means of the single-layer boundary integral

$$u_i(\mathbf{x}) = \int_S \phi_j(\xi) G_{ij}(\mathbf{x}, \xi) dS_\xi, \tag{1}$$

where  $u_i(\mathbf{x})$  is the *i*th component of the displacement at point  $\mathbf{x}$ ,  $G_{ij}(\mathbf{x}, \xi)$  is the Green's function, that is, the displacement produced in the direction *i* at  $\mathbf{x}$  due to the application of a unit force at point  $\xi$  in the direction *j*, and  $\phi_j(\xi)$  is the force density in the direction *j* at point  $\xi$ . Therefore, the product  $\phi_j(\xi) dS_\xi$  in the integral is a force distribution over the surface *S*. The subscript in the differential shows the space variable over which the integration is carried out. This integral representation for displacements can be obtained from Somigliana's identity (see Sánchez-Sesma & Campillo 1991) and was studied by Kupradze (1963), who showed that if  $\phi_j(\xi)$  is continuous over *S*, then the displacement field is continuous across *S*.

With the application of Hooke's law, one can compute the stresses and tractions, except at boundary singularities, that is, when  $\mathbf{x}$  is equal to  $\xi$  on surface *S*. From a limiting process based on equilibrium considerations around an internal neighbourhood of the boundary, it is possible to write, for  $\mathbf{x}$  on *S*,

$$t_i(\mathbf{x}) = c\phi_i(\mathbf{x}) + \int_S \phi_j(\xi) T_{ij}(\mathbf{x}, \xi) dS_\xi, \tag{2}$$

where  $t_i$  is the *i*th component of traction at the boundary,  $c =$

$1/2$  or  $c = -1/2$  if  $\mathbf{x}$  tends to *S* from inside the region or  $\mathbf{x}$  tends to *S* from outside the region, respectively, and  $T_{ij}(\mathbf{x}, \xi)$  is the traction Green's function. The first term of the right-hand side of eq. (2) must be equal to zero if  $\mathbf{x}$  is not on the surface *S*. The expressions for the Green's functions in a 3-D full-space can be found in Appendix A.

The problem that we want to solve is the diffraction of elastic waves by topographic features on the surface of an elastic half-space, as shown in Fig. 1, where the coordinate system is also presented. Surface motion in and around this irregular configuration comes from the interference of incoming, reflected and diffracted wavefields. The total motion in the half-space may be expressed as the superposition of the diffracted and the free wavefields:

$$u_i = u_i^{(d)} + u_i^{(0)}, \tag{3}$$

where the free-field displacement  $u_i^{(0)}$  is the solution in the absence of the irregularity and contains the contributions of both the incident and reflected fields. This displacement is extended to those parts of elevated topographies where  $z < 0$  (see Fig. 1 for a definition of the *z*-axis), fulfilling the same

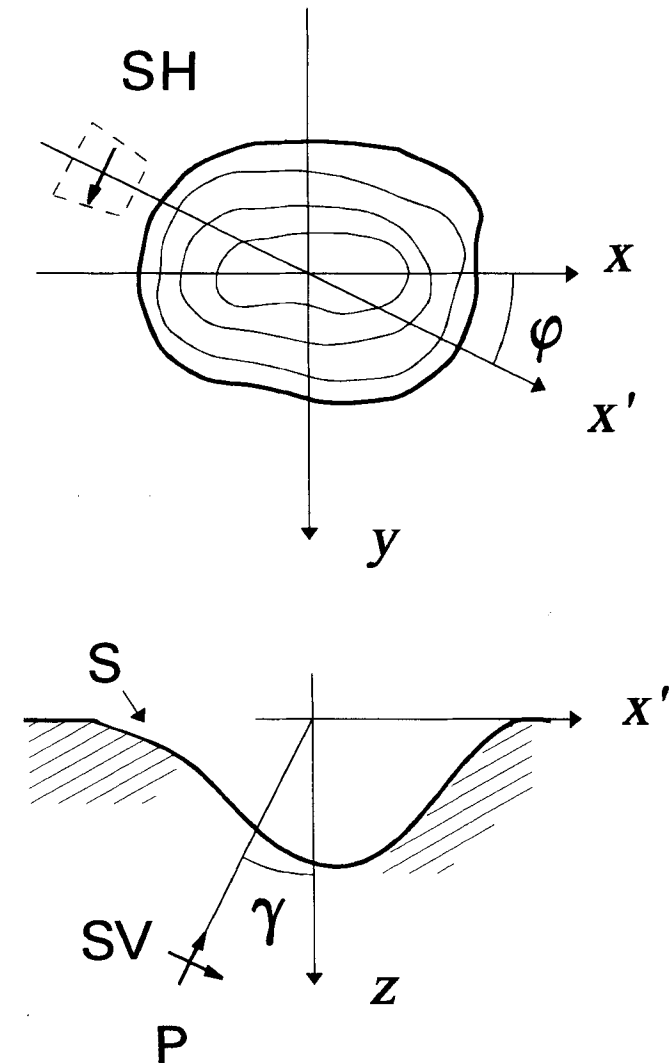


**Figure 1.** Surface topographic feature *S* in an elastic half-space under incidence of *P* and *S* waves with an angle  $\gamma$  with respect to the vertical and an azimuth equal to  $\phi$ .

analytical expressions that they satisfy for  $z \geq 0$ . Therefore, the free field is continuous everywhere.

According to eq. (1), the diffracted field can be written as

$$u_i^{(d)}(\mathbf{x}) = \int_S \phi_j(\xi) G_{ij}(\mathbf{x}, \xi) dS_\xi. \tag{4}$$

The traction-free boundary condition implies null tractions, and therefore from eq. (2) this condition can be expressed by means of

$$t_i^{(0)}(\mathbf{x}) + \frac{1}{2} \phi_i(\mathbf{x}) + \int_S \phi_j(\xi) T_{ij}(\mathbf{x}, \xi) dS_\xi = 0, \tag{5}$$

which is a Fredholm integral equation of the second kind for the boundary sources, that is, those producing the diffracted field. This expression is discretized over a finite portion of the surface  $S$  that includes the topography and part of the lateral flat free surface. This is an advantage, particularly if one considers the relatively large discretizations needed for techniques such as finite differences or finite elements, because the problem is reduced by one dimension. The lateral extension of the discretized flat part of the topography must be large enough to avoid significant spurious waves generated at the edges of the model. We concluded after several tests that the results were quite good when this part has the same length as the characteristic horizontal dimension  $a$  of the topography. Therefore, in the examples treated here the discretization of the free surface is extended over a distance  $2a$ . A simplified scheme to discretize the surface using circles of various sizes that approximately cover the surface  $S$  is used. This choice is based on the fact that the integrals of the Green's functions  $G_{ij}(\mathbf{x}, \xi)$  that must be computed when  $\mathbf{x}$  is near  $\xi$  can easily be obtained when the discretized element is circular and flat. Nevertheless, in order to partially overcome the effects of this approximate discretization scheme, we use at least four aligned boundary elements per wavelength of  $S$  waves.

Considering  $\phi_j(\xi)$  to be constant over each of the boundary circular elements obtained in the discretization process, and denoting the surface of each by  $\Delta S_p$  ( $p = 1, \dots, N$ ), the following system of  $3N$  linear equations, with  $3N$  unknowns, is obtained for these boundary sources:

$$\sum_{p=1}^N \phi_j(\xi_p) t_{ij}(\mathbf{x}_q, \xi_p) = -t_i^{(0)}(\mathbf{x}_q), \quad q = 1, \dots, N, \tag{6}$$

with

$$t_{ij}(\mathbf{x}_q, \xi_p) = \frac{1}{2} \delta_{ij} \delta_{qp} + \int_{\Delta S_p} T_{ij}(\mathbf{x}_q, \xi) dS_\xi. \tag{7}$$

These integrals are computed numerically except when  $\mathbf{x} = \xi$ , in which case we obtain

$$t_{ij}(\mathbf{x}_q, \xi_q) = \frac{1}{2} \delta_{ij}, \tag{8}$$

because the integral of the Green's tensor  $T_{ij}$  in eq. (7) is zero if the integrated surface  $\Delta S_p$  is circular and flat, which is the case assumed here. In fact, the integrand is a singular odd function on this surface, and therefore its Cauchy principal value is null. Once the values of  $\phi_j(\xi_p)$  are calculated, the diffracted field at a position  $\mathbf{x}$  can be computed by means of the discretized version of the integral representation for displacements

$$u_i^{(d)}(\mathbf{x}) = \sum_{p=1}^N \phi_j(\xi_p) g_{ij}(\mathbf{x}, \xi_p), \tag{9}$$

where

$$g_{ij}(\mathbf{x}, \xi_p) = \int_{\Delta S_p} G_{ij}(\mathbf{x}, \xi) dS_\xi. \tag{10}$$

These integrals are also computed numerically except if  $\mathbf{x}$  is in the neighbourhood of  $\xi_p$ . In that case, we used analytical integration in polar coordinates of the ascending power series for the functions  $f_1$  and  $f_2$  that appear in the expression for the Green's function. On the other hand, when  $\mathbf{x} = \xi_p$ , that is, in the centre of the  $p$ th circular element, it is possible to show that

$$\int_{\Delta S_p} G_{ij}(\mathbf{x}, \xi) dS_\xi = \frac{1}{4\mu} [(F_2 + F_1) \delta_{ij} + (F_2 - F_1) n_i n_j], \tag{11}$$

where  $F_k$ ,  $k=1,2$ , is the integral of the function  $f_k$ , from zero to the radius of the element, and  $n_j$  is the  $j$ th component of the normal vector at the  $p$ th element.

### DIFFRACTION OF ELASTIC WAVES BY 3-D TOPOGRAPHIES

We compare results obtained from our numerical technique when it is applied to the problem of the diffraction of elastic waves by a hemispherical cavity. This configuration was studied earlier by Sánchez-Sesma (1983) using an approach based on multipolar wave expansions in spherical coordinates, and by Mossesian & Dravinski (1989), who relied on an indirect boundary integral equation method.

The comparison among these three solutions is made for vertically incident  $P$  waves at a normalized frequency  $\eta = 2(a\beta/f)$  of 0.866, where  $a$  is the radius of the cavity,  $\beta$  denotes the  $S$ -wave velocity and  $f$  is the frequency. The half-space properties are set so that the Poisson's ratio  $\nu = 1/4$ . The discretization is extended horizontally up to a radius of  $2a$ . Displacement amplitudes are shown in Fig. 2 and are plotted along the  $x$ -axis from  $x = -2a$  to  $x = +2a$ . The results of the three techniques show some small discrepancies, but the overall agreement is quite good. We obtain similar good agreement in other comparisons, not shown here, for incident  $S$  waves and different frequencies.

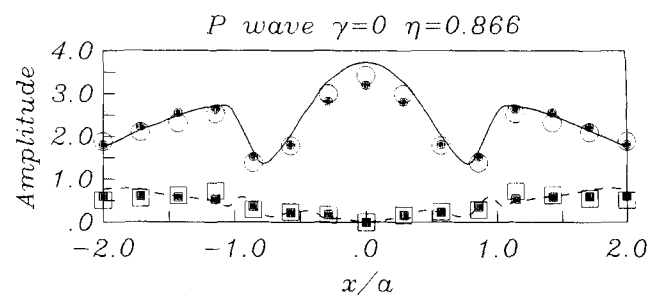


**Figure 2.** Surface amplitudes for the horizontal,  $u$ , and vertical,  $w$ , displacements due to a vertically incident  $P$  wave on a hemispherical cavity. Normalized frequency  $\eta = 0.866$ . Material properties are given in the text. Surface displacement amplitudes are plotted along the  $x$ -axis from  $x = -2a$  to  $x = +2a$ . Mossesian & Dravinski's (1989) results are shown as filled symbols and those of Sánchez-Sesma (1983) are shown as empty symbols. Our solution is depicted by solid and dashed lines for the  $w$  and  $u$  motions, respectively.

We now study the cases of a cavity and a mountain to investigate some effects caused by 3-D topographies. Results in the frequency and time domains are shown for the surface displacements in two perpendicular cross-sections ( $x=0$  and  $y=0$ ). We illustrate the results in the frequency domain by means of  $f-x$  plots. In this way one can analyse the transfer function (relative to the amplitude of incident waves) along a specified space direction and also as a function of the frequency. This provides spatial patterns of amplification. The time displacements are computed using the FFT algorithm. We also present polarigrams of motion for the case of a mountain topography. They are helpful in the interpretation and identification of travelling waves; see Luzón *et al.* (1995).

**Cylindrical cavity and incident SV and Rayleigh waves**

In this example, we compute the response of a cylindrical cavity (as depicted in Fig. 3) under incoming SV and Rayleigh waves. The radius of this cavity is set equal to 4 km and the depth equal to 1 km. The material properties are such that  $\beta=2.5 \text{ km s}^{-1}$  and the Poisson's ratio  $\nu=1/3$ . No damping is considered, and an incidence angle  $\gamma=30^\circ$  with azimuth  $\phi=0^\circ$  is assumed for SV waves. The discretization of the flat surface of the model, with 368 circular elements, is carried out from a radius of 4 km to a radius of 8 km from the origin. The cavity has 64 elements that cover the cylindrical wall and 145 that cover the flat base.

Figs 4 and 5 show the contours of surface amplitudes produced along the  $x$ -axis, that is, the  $u$  and  $w$  displacements, respectively, caused by incoming SV waves. In both plots the space variable goes from  $x=-8 \text{ km}$  to  $x=+8 \text{ km}$ , and the frequency range extends from 0 to 1.2 Hz. Zero frequency corresponds to the case when there is no topographical irregularity. For the  $u$  component, the amplitude produced over the flat surface that lies to the left of the cavity, from  $x=-8 \text{ km}$  to  $x=-4 \text{ km}$ , is much larger, due to the constructive interference of direct and scattered waves, than the amplitude in the region located to the right of the cavity (*shadow effect*). Inside the cavity this phenomenon is reversed and the largest amplitude occurs in the cavity region opposite to the direction of the incoming waves. This effect is more pronounced for the

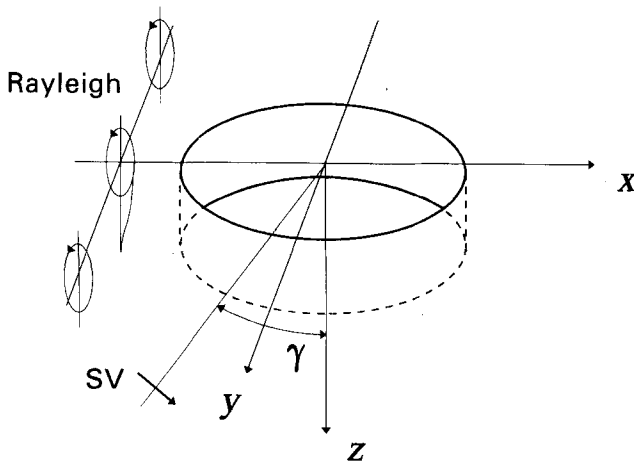


**Figure 3.** Cylindrical cavity in a half-space under incidence of SV and Rayleigh waves.

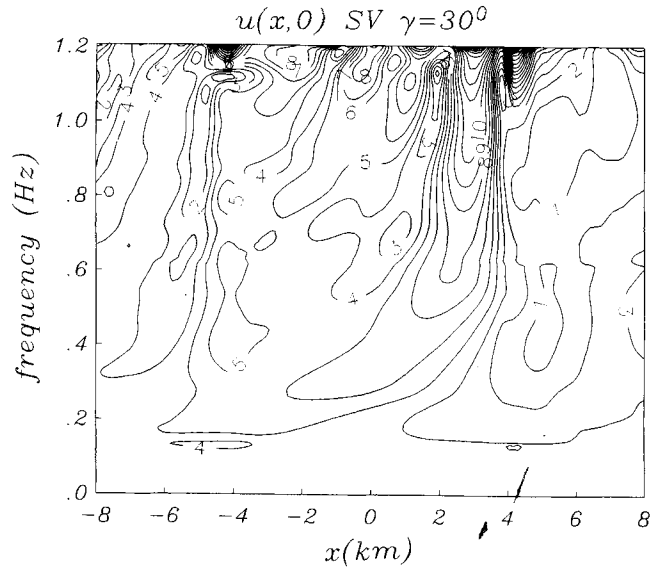


**Figure 4.** Contours of horizontal displacement amplitude  $u$  for surface receivers along the  $x$ -axis against frequency for a cylindrical cavity under incoming SV waves with an incident angle of  $30^\circ$  with respect to the vertical.

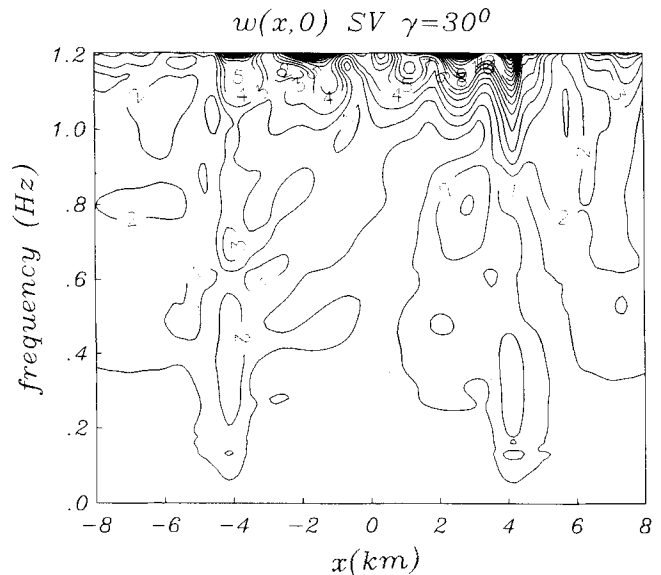


**Figure 5.** Contours of vertical displacement amplitude  $w$  for surface receivers along the  $x$ -axis against frequency for a cylindrical cavity under incoming SV waves with an incident angle of  $30^\circ$  with respect to the vertical.

higher frequencies, and the largest amplitudes are then observed at the edge of the cavity. This remarkable effect is also present for the vertical displacement  $w$ . In this case, the maximum amplitudes are produced over the positive values of the  $x$ -axis.

We computed synthetic seismograms for the configuration described above using a Ricker wavelet with a characteristic period of  $t_p=2 \text{ s}$ . These time-series calculated at 49 receivers along the  $x$ -axis and 49 along the  $y$ -axis are displayed in Fig. 6. Their positions are equally spaced between  $x=-7.68 \text{ km}$  (or

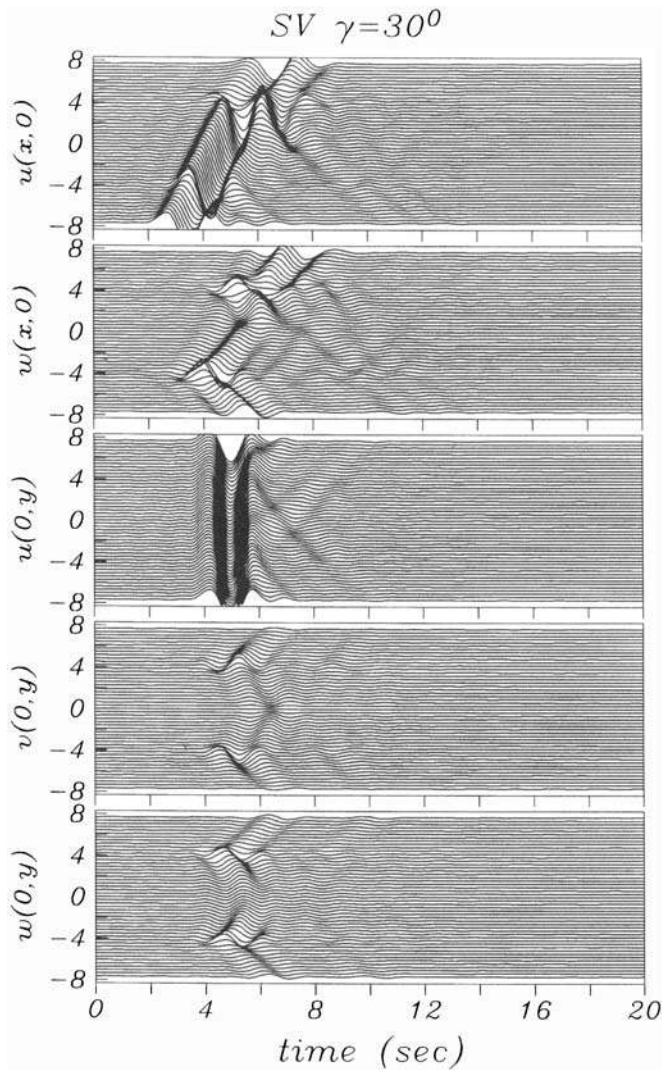


**Figure 6.** Synthetic seismograms for displacement at 98 points for a cylindrical cavity under incoming *SV* waves with an incident angle of  $30^\circ$  with respect to the vertical. 49 receivers are equally spaced along the  $x$ -axis between  $x = -7.68$  km and  $x = 7.68$  km, and another 49 receivers are equally spaced along the  $y$ -axis between  $y = -7.68$  km and  $y = 7.68$  km. The incident waveform is a Ricker wavelet with characteristic period  $t_p = 2$  s.

$y = -7.68$  km) and  $x = 7.68$  km (or  $y = 7.68$  km). The displacement  $u$  at receivers located along the  $x$ -axis, represented by  $u(x,0)$ , shows the amplification effects observed in the frequency domain. For example, inside the cavity and near the edge, at  $x = 4$  km, a large amplification can be seen to originate from constructive interference between direct and scattered waves. The latter waves also propagate back and forth across the cavity from the curved edge. On the other hand, the seismograms of displacement  $u$  along the  $y$ -axis,  $u(0,y)$ , clearly show the emission of diffracted waves from the cavity's edge. These waves are produced by a mode-conversion process, and propagate as *SH*-wave energy. The displacements  $w$  along both axes and  $v$  along the  $y$ -axis are the consequence of the diffracted waves radiated from the walls of the cavity, which behave as very efficient diffractors. In fact, vertical walls may be very efficient in the generation of diffracted waves, as shown by

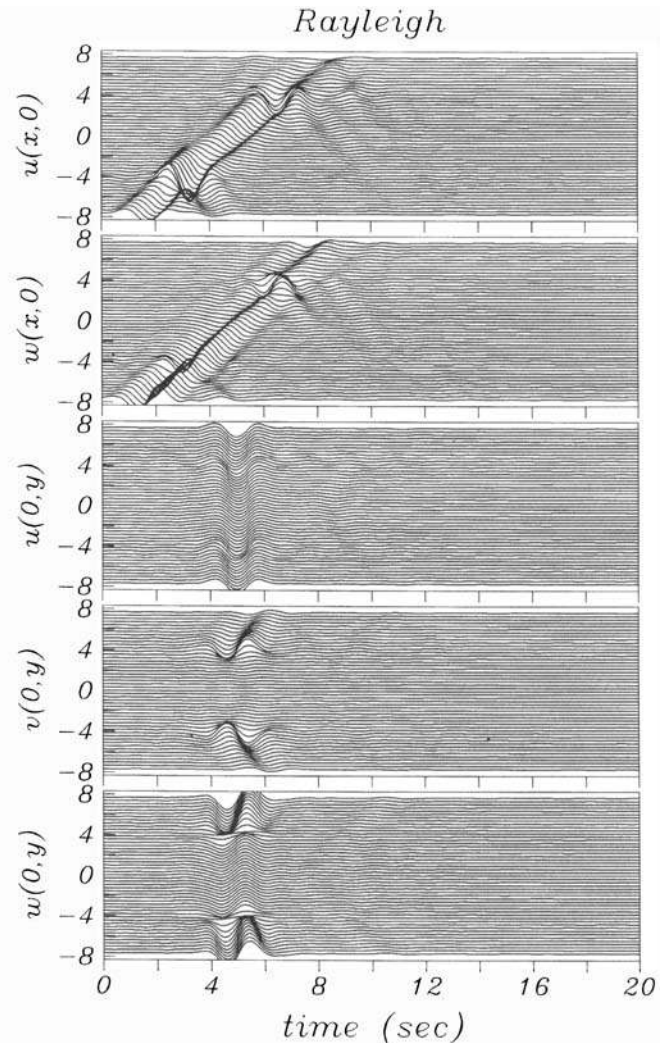


**Figure 7.** Synthetic seismograms for displacement at 98 points for a cylindrical cavity under incoming Rayleigh waves. 49 receivers are equally spaced along the  $x$ -axis between  $x = -7.68$  km and  $x = 7.68$  km, and another 49 receivers are equally spaced along the  $y$ -axis between  $y = -7.68$  km and  $y = 7.68$  km. The incident waveform is a Ricker wavelet with a characteristic period  $t_p = 2$  s.

Yokoi (1996) in the analysis of a series of field experiments. In our example, the waves that propagate away from the topographic structure are Rayleigh surface waves, while those propagating inside are the so-called creeping waves (see e.g. Kawase 1988; Sánchez-Sesma & Campillo 1991).

The results obtained in the case of incidence of Rayleigh waves are presented in Fig. 7. The locations of the receivers and the displacement components shown are the same as in the *SV*-incidence case. The motion along the  $x$ -axis is characterized by the backward propagation of Rayleigh waves from the edges of the topography, and by the deamplification occurring at the rear side of the cavity due to the shadow effect.

#### A mountain and incident *P* and *S* waves

In this example, the topographical region that we study is defined in the interior of a circumference of radius  $a$ , centred at the origin  $(x,y) = (0,0)$ , minus the shared region with a

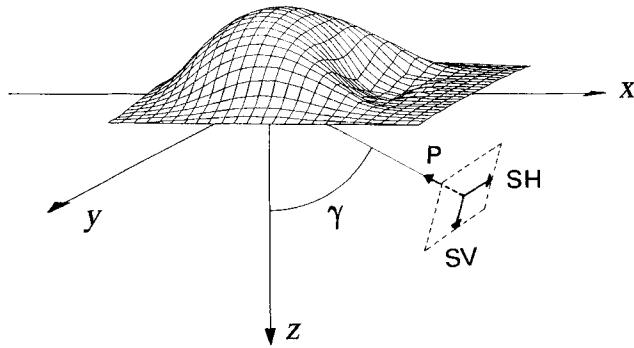


**Figure 8.** Perspective view of the 3-D mountain. The incoming  $P$  and  $S$  waves have an azimuth  $\varphi = \pi$  radians and an incidence angle  $\gamma$  with respect to the vertical.

circumference of radius  $b$ , centred at  $(x, y) = (a, 0)$ , with  $a > b$ . The surface geometry of the mountain is given by the analytical expression

$$z(x, y) = c(R^2 - b^2) \left( 1 - \frac{2a(a-x)}{R^2} \right), \quad (12)$$

where  $R = [(x-a)^2 + y^2]^{1/2}$ , and  $c$  is a parameter that controls the height. As we have selected  $b = 0.7a$  and  $c = 0.4/a$ , the maximum height is near  $0.25a$ . This topography is depicted in Fig. 8, showing incoming  $P$  and  $S$  plane waves with an azimuth  $\varphi = \pi$  radians and an incidence angle  $\gamma$ .

Here we present results for  $\gamma = 30^\circ$ . The value for  $a$  is assumed to be 2 km, so the top of the mountain is about 0.5 km. Material properties are such that  $\beta = 1 \text{ km s}^{-1}$ ,  $\nu = 0.25$  and the quality factor  $Q$  is 500 for both  $P$  and  $S$  waves. The surface of the mountain is constructed with 145 circular elements, and the flat part of the model has 232 elements. We computed synthetic seismograms and considered for the incoming wave a Ricker wavelet with a characteristic period of  $t_p = 3 \text{ s}$ . Results are depicted in Figs 9, 10 and 11 for incident  $P$ ,  $SV$  and  $SH$  waves, respectively. In these plots we depict all the surface displacements different from zero along the  $x$ - and  $y$ -axes. The emission of waves from the irregularity is very important. Backward and forward propagation of Rayleigh waves are produced by incident  $P$  and  $SV$  waves. These surface waves generated by diffraction have a higher energy when they propagate in the same direction as the incoming field. The presence of these waves in the direction perpendicular to the plane of incidence [ $v(0, y)$  and  $w(0, y)$ ] suggests that they are radiated in all directions. We present in Fig. 12 some polarigrams, which display the variation of the displacement vectors with time, for the  $SV$ -wave incidence. The Rayleigh waves can be clearly identified in the later arrivals by their characteristic elliptical and retrograde motion.

## CONCLUSIONS

We have applied a simplified indirect boundary element method to compute the response of 3-D topographies over the surface of an elastic half-space under incoming  $P$ ,  $S$  and Rayleigh waves. This mathematical technique, which is based on an integral representation of diffracted fields, can be seen as a numerical realization of Huygens' principle because

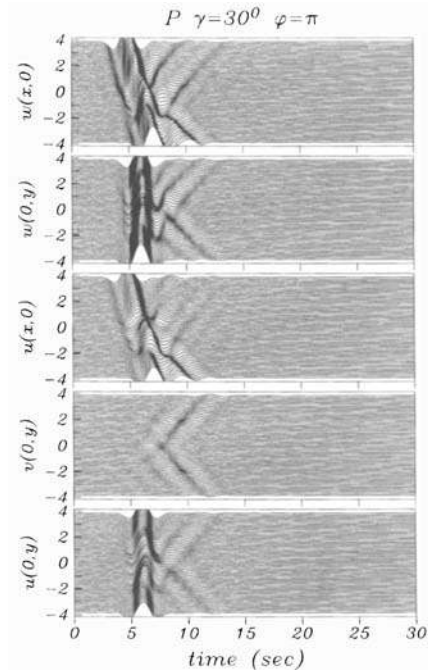


**Figure 9.** Synthetic seismograms for  $u$ ,  $v$  and  $w$  at 49 receivers equally spaced along the  $x$ - or  $y$ -axis at a mountain under incoming  $P$  waves with an incidence angle of  $30^\circ$  and an azimuth of  $\pi$  radians. The range of locations of receivers on the  $x$ - or  $y$ -axis is between  $-3.84 \text{ km}$  and  $3.84 \text{ km}$ . The incident waveform is a Ricker wavelet with a characteristic period  $t_p = 3 \text{ s}$ .

diffracted waves are constructed at the boundaries, from where they are radiated by means of boundary sources.

We have studied the seismic response of a flat cylindrical cavity to incoming  $P$ ,  $S$  and Rayleigh waves. The principal characteristics inferred are the following:

- (1) the walls of the cylindrical cavity are very good diffractors, producing an emission of energy in all directions;
- (2) a large part of this energy was identified as Rayleigh waves.

In another example, we have investigated the effect of a mountain topography on  $P$  and  $S$  waves. The results in the time domain have provided us with a glimpse of the origin of the amplifications or attenuations of surface displacements. This understanding has been achieved by means of a polarization analysis of particle motion and the estimation of apparent wave velocity. The interference between diffracted Rayleigh waves, creeping waves and waves generated by mode conversion produces complicated patterns in displacement amplitudes.

The indirect boundary element method presented is very efficient and no approximations are necessary in its implementation, except in the discretization process. Any geometry can be handled and any type of plane wave, regardless of the incidence angle or azimuth, can be considered. Moreover, in this technique it is relatively simple to include near-source effects, by changing the free-field in eq. (3) to include the source field. The limitations of the technique are related to the size of the matrix obtained from the system of linear equations,

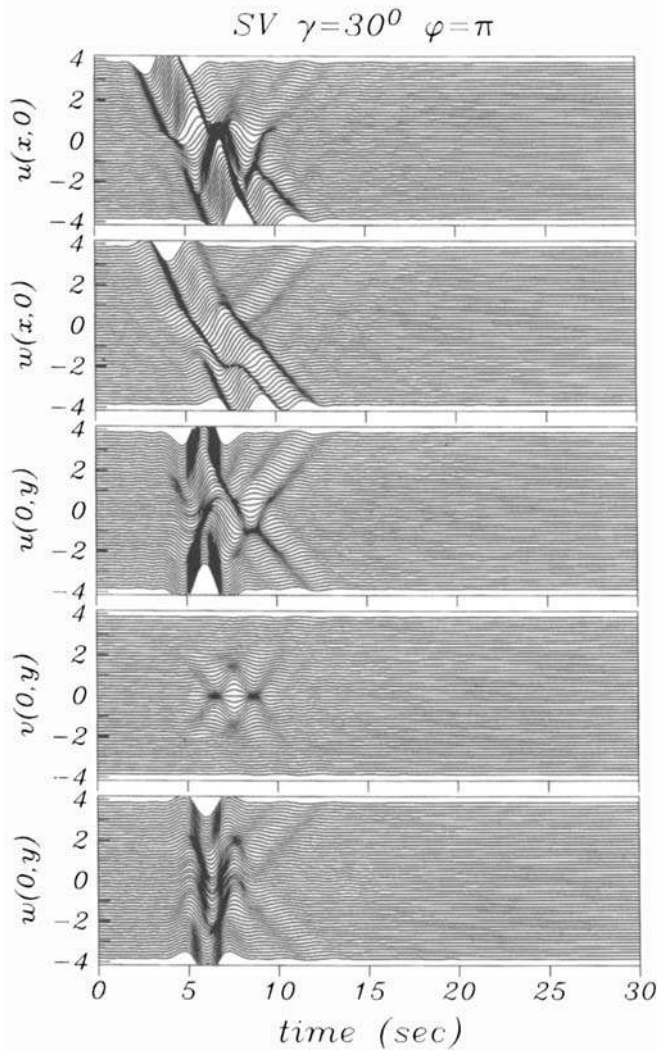


Figure 10. Same as Fig. 9 with incidence of SV waves.

and consequently to the CPU time; the number of elements in the matrix depends on the number of discretized elements, which increases with frequency. In any event, this matrix has relatively few elements at frequencies for which the associated wavelengths are comparable to the characteristic dimensions of many real topographies. On the other hand, the use of the Green's functions of the full-space implicitly limits the technique as we can only compute the response of topographies on top of a homogeneous half-space. Nevertheless, with this technique and with appropriate Green's functions it is still possible to take into account a layered structure or a medium with a velocity gradient, for example.

**ACKNOWLEDGMENTS**

Thanks are given to F. Vidal and M. Bouchon for the critical reading of the manuscript and many useful suggestions. The comments of an unknown reviewer helped to improve this article. This work was partially supported by CICYT, Spain, under grants ANT95-0994-C03-02 and SEC94-0633, by the research team of *Geofisica Aplicada* of Junta de Andalucía, Spain, by Secretaría General de Obras del Departamento del

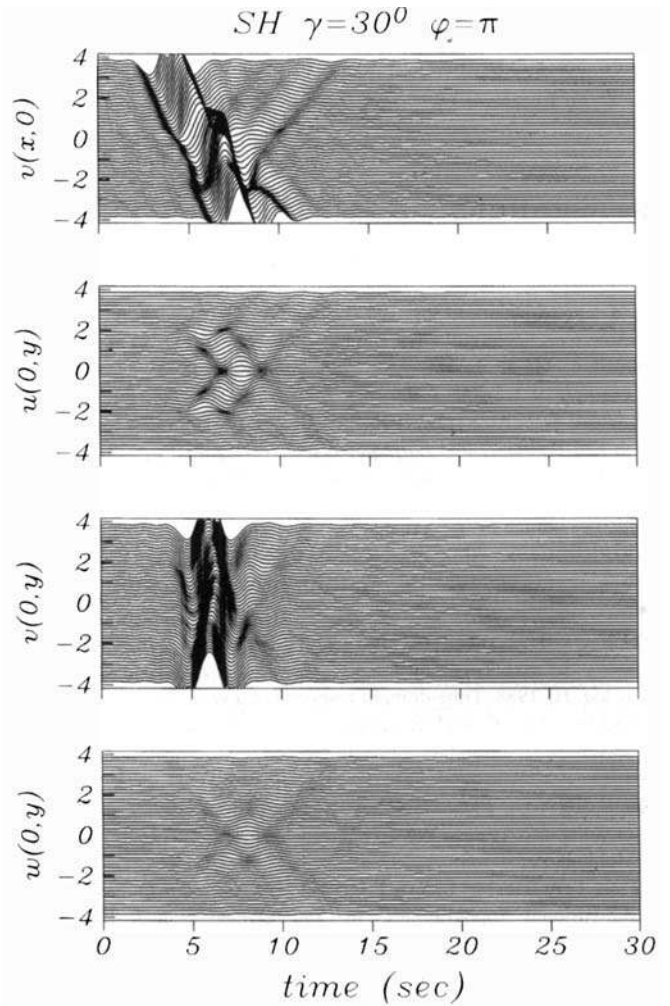


Figure 11. Same as Fig. 9 with incidence of SH waves.

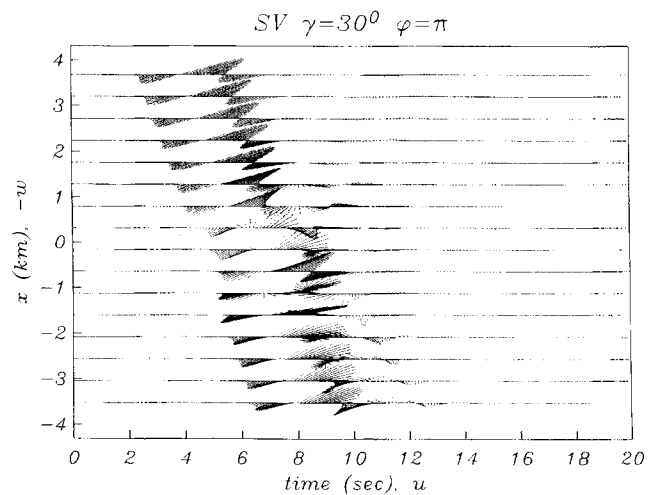


Figure 12. Polarigrams at 16 receivers equally spaced along the x-axis. The time and the horizontal displacements *u* on the abscissa are plotted against the position over the free surface of the configuration and the vertical displacements *w* on the ordinate axis.

Distrito Federal, México, by Consejo Nacional de Ciencia y Tecnología, México, by Dirección General de Asuntos del Personal Académico of UNAM, under grant IN108295, and by Cray Research Inc., under grant SC-100894.

## REFERENCES

- Aki, K., 1988. Local site effects on strong ground motion, in *Earthquake Engineering and Soil Dynamics II—Recent Advances in Ground Motion Evaluation*, pp. 103–155, ed. Lawrence Von Thun, J., American Society of Civil Engineering, New York, NY.
- Bouchon, M. & Barker, J.S., 1996. Seismic response of a hill: the example of Tarzana, California, *Bull. seism. Soc. Am.*, **86**, 66–72.
- Clouteau, D. & Aubry, D., 1995. Site effects on 3D elevated topography, in *Soil Dynamics and Earthquake Engineering VII*, pp. 291–298, eds Cakmak, A.S. & Brebbia, C.A., Computational Mechanics Publications, Southampton.
- Fäh, D., Suhadolc, P., Mueller, St. & Panza, G.F., 1994. A hybrid method for the estimation of ground motion in sedimentary basins: quantitative modeling for Mexico city, *Bull. seism. Soc. Am.*, **84**, 383–399.
- Furumara, T. & Takenaka, H., 1996. 2.5-D modelling of elastic waves using the pseudospectral method, *Geophys. J. Int.*, **124**, 820–832.
- Kawase, H., 1988. Time-domain response of a semicircular canyon for incident SV, P, and Rayleigh waves calculated by the discrete wavenumber boundary element method, *Bull. seism. Soc. Am.*, **78**, 1415–1437.
- Kupradze, V.D., 1963. Dynamical problems in elasticity, in *Progress in Solid Mechanics*, Vol. 3, eds Sneddon, I.N. & Hill, R., North Holland, Amsterdam.
- Luzón, F. & Sánchez-Sesma, F.J., 1995. The seismic response of three-dimensional topographies, in *Soil Dynamics and Earthquake Engineering VII*, pp. 247–258, eds Cakmak, A.S. & Brebbia, C.A., Computational Mechanics Publications, Southampton.
- Luzón, F., Aoi, S., Fäh, D. & Sánchez-Sesma, F.J., 1995. Simulation of the seismic response of a 2D sedimentary basin: a comparison between the indirect boundary element method and a hybrid technique, *Bull. seism. Soc. Am.*, **85**, 1501–1506.
- Manolis, G.D. & Beskos, D.E., 1988. *Boundary Element Methods in Elastodynamics*, Unwin Hyman Ltd, London.
- Mossessian, T.K. & Dravinski, M., 1989. Scattering of elastic waves by three-dimensional surface topographies, *Wave Motion*, **11**, 579–592.
- Olsen, K.B., Archuleta, R.J. & Matarese, J.R., 1995. Three-dimensional simulation of a magnitude 7.75 earthquake on the San Andreas fault, *Science*, **270**, 1628–1632.
- Pedersen, H.A., Maupin, V. & Campillo, M., 1996. Wave diffraction in multilayered media with the indirect boundary element method: application to 3-D diffraction of long-period surface waves by 2-D lithospheric structures, *Geophys. J. Int.*, **125**, 545–558.
- Sánchez-Sesma, F.J., 1983. Diffraction of elastic waves by three-dimensional surface irregularities, *Bull. seism. Soc. Am.*, **73**, 1621–1636.
- Sánchez-Sesma, F.J., 1996. Strong ground motion and site effects, in *Computer Analysis and Design of Earthquake Resistant Structures*, eds Beskos, D.E. & Anagnostopoulos, S.A., Computational Mechanics Publications, Southampton, in press.
- Sánchez-Sesma, F.J. & Campillo, M., 1991. Diffraction of P, SV and Rayleigh waves by topographic features: a boundary integral formulation, *Bull. seism. Soc. Am.*, **81**, 2234–2253.
- Sánchez-Sesma, F.J. & Luzón, F., 1995. Seismic response of three dimensional alluvial valleys for incident P, S and Rayleigh waves, *Bull. seism. Soc. Am.*, **85**, 269–284.
- Sánchez-Sesma, F.J. & Rosenbluth, E., 1979. Ground motion at

canyons of arbitrary shape under incident SH waves, *Int. J. Earthq. Eng. struct. Dyn.*, **7**, 441–450.

Sánchez-Sesma, F.J., Ramos-Martínez, J. & Campillo, M., 1993. An indirect boundary element method applied to simulate the seismic response of alluvial valleys for incident P, S and Rayleigh waves, *Earthq. Eng. struct. Dyn.*, **22**, 279–295.

Takenaka, H., Kennett, B.L.N. & Fujiwara, H., 1996. Effect of 2-D topography on the 3-D seismic wavefield using a 2.5-D discrete wavenumber–boundary integral equation method, *Geophys. J. Int.*, **124**, 741–755.

Yokoi, T., 1996. Numerical study on the generation of downgoing S-waves by a vertical force acting close to a step-like topography, *Geophysics*, **61**, 192–201.

## APPENDIX A: 3-D GREEN'S FUNCTIONS IN A FULL-SPACE

The displacement Green's functions, for harmonic/time dependence  $e^{i\omega t}$ , with  $i$  the imaginary unity,  $\omega$  the circular frequency and  $t$  the time, in a homogeneous elastic full-space, can be written as

$$G_{ij}(\mathbf{x}, \xi) = \frac{1}{4\pi\mu r} [f_2\delta_{ij} + (f_1 - f_2)\gamma_i\gamma_j], \quad (\text{A1})$$

where  $r^2 = (x_1 - \xi_1)^2 + (x_2 - \xi_2)^2 + (x_3 - \xi_3)^2$  and  $\gamma_j = (x_j - \xi_j)/r$ ,  $\mu = \rho\beta^2$ , with  $\rho$  the mass density and  $\beta$  the S-wave velocity, and  $\delta_{ij}$  is Kröonecker's delta. The functions  $f_1$  and  $f_2$  are defined as

$$f_1 = \frac{\beta^2}{\alpha^2} \left[ 1 - \frac{2i}{qr} - \frac{2}{(qr)^2} \right] e^{-iqr} + \left[ \frac{2i}{kr} + \frac{2}{(kr)^2} \right] e^{-ikr}, \quad (\text{A2})$$

$$f_2 = \frac{\beta^2}{\alpha^2} \left[ \frac{i}{qr} + \frac{1}{(qr)^2} \right] e^{-iqr} + \left[ 1 - \frac{i}{kr} - \frac{1}{(kr)^2} \right] e^{-ikr}, \quad (\text{A3})$$

where  $k = \omega/\beta = S$  wavenumber,  $q = \omega/\alpha = P$  wavenumber and  $\alpha$  is the P-wave velocity.

The Green's tractions are given by

$$T_{ij} = \frac{1}{4\pi r^2} [(g_1 - g_2 - 2g_3)\gamma_i\gamma_j n_k n_k + g_3\gamma_i n_j + g_2\gamma_j n_i + g_3\gamma_k n_k \delta_{ij}], \quad (\text{A4})$$

where the functions  $g_j$ ,  $j = 1, 2, 3$ , are expressed as

$$g_j = [krA_{1j} + B_{1j} + \frac{C_{1j}}{kr} + \frac{D_{1j}}{(kr)^2}] e^{-ikr} + [krA_{2j} + B_{2j} + \frac{C_{2j}}{kr} + \frac{D_{2j}}{(kr)^2}] e^{-iqr}. \quad (\text{A5})$$

The coefficients of this expression are given in Table A1.

**Table A1.** Coefficients of the functions  $g_j$  of eq. (A5).

	$j = 1$	$j = 2$	$j = 3$
$A_{1j}$	0	0	$-i$
$A_{2j}$	$-i\beta/\alpha$	$i(2\beta^3/\alpha^3 - \beta/\alpha)$	0
$B_{1j}$	4	-2	-3
$B_{2j}$	$-4\beta^2/\alpha^2 - 1$	$4\beta^2/\alpha^2 - 1$	$2\beta^2/\alpha^2$
$C_{1j}$	-12i	6i	6i
$C_{2j}$	$12i\beta/\alpha$	$-6i\beta/\alpha$	$-6i\beta/\alpha$
$D_{1j}$	-12	6	6
$D_{2j}$	12	-6	-6